# A Finite Element Study of Elasto-Plastic Hemispherical Contact Against a Rigid Flat

**Robert L. Jackson**[1]
Member, ASME

**Itzhak Green**
Fellow, ASME

George W. Woodruff School of Mechanical Engineering,
Georgia Institute of Technology,
Atlanta, GA 30332-0405
e-mail: gt2433a@prism.gatech.edu

*This work presents a finite element study of elasto-plastic hemispherical contact. The results are normalized such that they are valid for macro contacts (e.g., rolling element bearings) and micro contacts (e.g., asperity contact), although micro-scale surface characteristics such as grain boundaries are not considered. The material is modeled as elastic-perfectly plastic. The numerical results are compared to other existing models of spherical contact, including the fully plastic truncation model (often attributed to Abbott and Firestone) and the perfectly elastic case (known as the Hertz contact). This work finds that the fully plastic average contact pressure, or hardness, commonly approximated to be a constant factor of about three times the yield strength, actually varies with the deformed contact geometry, which in turn is dependent upon the material properties (e.g., yield strength). The current work expands on previous works by including these effects and explaining them theoretically. Experimental and analytical results have also been shown to compare well with the current work. The results are fit by empirical formulations for a wide range of interferences (displacements which cause normal contact between the sphere and rigid flat) and materials for use in other applications.*
[DOI: 10.1115/1.1866166]

## Introduction

The modeling of elasto-plastic hemispheres in contact with a rigid surface is important in contact mechanics on both the macro and micro scales. This work presents a dimensionless model that is valid for both scales, although micro-scale surface characteristics such as grain boundaries are not considered. In the former, e.g., rolling element bearings, load may be high and the deformations excessive. In the latter, e.g., asperity contact, a model on the micro-scale is of great interest to those investigating friction and wear. In addition, the real area of contact of such asperities will affect the heat and electrical conduction between surfaces. In either scale contact is often modeled as a hemisphere against a rigid flat. Much interest is devoted in the literature to the reverse case of indentation loading where a rigid sphere penetrates an elasto-plastic half-space. It is worthy to emphasize that indentation (other works) and hemispherical deformation (this work) are significantly different in the elasto-plastic and fully plastic regimes, and only the latter is the subject of this work.

One of the earliest models of elastic asperity contact is that of Greenwood and Williamson [1]. This (GW) model uses the solution of the frictionless contact of an elastic hemisphere and a rigid flat plane, otherwise known as the Hertz contact solution [2], to stochastically model an entire contacting surface of asperities with a postulated Gaussian height distribution. The GW model assumes that the asperities do not interfere with adjacent asperities and that the bulk material below the asperities does not deform. The Gaussian distribution is often approximated by an exponential distribution to allow for an analytical solution, although Green [3] has analytically solved the integrals using the complete Gaussian height distribution. Supplementing the GW model, many elasto-plastic asperity models have been devised [4–8]. Appendix A provides a summary of these models. Many of these elasto-plastic models make use of the fully plastic Abbott and Firestone model [9], while Greenwood and Tripp derive a very similar model [10]. It should be noted that Abbott and Firestone [9] intended their model to be used to describe a wear process rather then a deformation process, but literature has still traditionally attributed this fully plastic truncation model to them (see Appendix A for a detailed description). Although these previous models have proven useful, they contain clear pitfalls which may be detrimental to their validity.

Additionally, the reversed case of a rigid spherical indentation of a deformable half-space has been thoroughly investigated experimentally [12–14] and numerically [15–19]. Work has also been done on the contact of a rigid cylinder contacting an elasto-plastic layered half-space [20]. More generally, various experimental and numerical works have investigated other contacting geometries and hardness tests [11,21,22]. The two works by Barber et al. [23] and Liu et al. [24] provide a more in-depth look at past and more recent findings in the field of contact mechanics. Perhaps a most important and relevant work is by Johnson [25], who experimentally measured the plastic strains between copper cylinders and spheres. Johnson's experimental results compare favorably with the findings of the current work. Despite the extensive body of works, the results, trends, and theories presented in the present work, to the authors' knowledge, have not yet been thoroughly documented.

The current work uses the finite element method to model the case of an elastic-perfectly plastic sphere in frictionless contact with a rigid flat (see Fig. 1). The von Mises criterion defines the yielding of the material. The resulting numerical data is also fitted by continuous functions that capture deformations all the way from purely elastic to fully plastic conditions. These expressions, which have a relatively low statistical error, may be used in other applications whether they are on macro or micro scales. For example, a statistical model for asperity contact (such as GW [1]) can greatly benefit from such expressions.

The finite element analysis presented in this work produced different results than the similar Kogut and Etsion (KE) model [4]. The current work accounts for geometry and material effects which are not accounted for in the KE model. Most notable of these effects is that the predicted hardness is not a material constant as suggested by Tabor [11] and many others; rather hardness changes with the evolving contact geometry and the material

[1]Currently at the Department of Mechanical Engineering, Auburn University, Auburn, AL, 36849; e-mail: robert.jackson@eng.auburn.edu

Contributed by the Tribology Division for publication in the ASME JOURNAL OF TRIBOLOGY. Manuscript received by the Tribology Division April 29, 2004; revised manuscript received September 8, 2004. Review conducted by: J. Tichy.

  

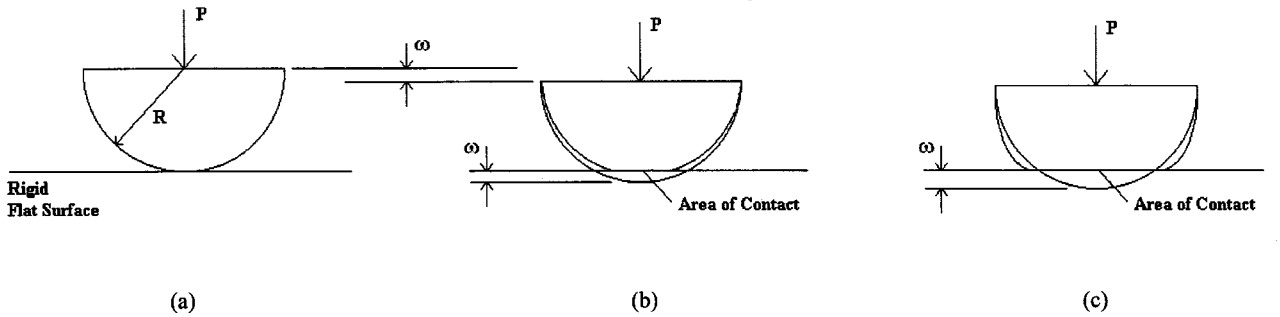


**Fig. 1 Spherical contact model before contact (*a*), during mostly elastic deformation (*b*), and during mostly plastic deformation (*c*)**

properties as proven in this work. Moreover, the current work uses a mesh that is orders of magnitude finer than that in [4] which was mandated by mesh convergence. The current work models deformation surpassing $\omega/\omega_c=110$ (the limit of KE), and likewise models five different material strengths, $S_y$, that showed a markedly different behavior in the transition from elasto-plastic to fully plastic deformation. The formulations derived in the current work are also continuous for the entire range of modeled interferences, whereas the KE model is discontinuous in two separate locations.

There is ambiguity and a lack of a universal definition of hardness. Not only are there various hardness tests for various scales and materials (Brinell, Rockwell, Vickers, Knoop, Shore, etc.), the *Metals Handbook* [12] defines hardness as ''Resistance of metal to plastic deformation, usually by indentation. However, the term may also refer to stiffness or temper, or to resistance to scratching, abrasion, or cutting. It is the property of a metal, which gives it the ability to resist being permanently, deformed (bent, broken, or have its shape changed), when a load is applied. The greater the hardness of the metal, the greater resistance it has to deformation.'' Another definition is that hardness measures the resistance to dislocation movement in the material, in which case it is directly related to the yield strength (and thus is interchangeable and perhaps redundant). A common definition that has gained status in the field is that hardness equals the average indentation pressure that occurs during fully plastic yielding of the contact area. As is shown in this work, hardness of this type of definition varies with the plastic and elastic properties and the contact geometry of the surface, i.e., with the deformation itself. A hardness geometric limit will be defined and discussed in the foregoing.

## Critical Interference

While in the elastic regime, the stresses within the hemisphere increase with $P$ and $\omega$. These stresses eventually cause the material within the hemisphere to yield. The interference at the initial point of yielding is known as the critical interference, $\omega_c$. The current work derives this critical interference analytically using the von Mises yield criterion (VM). The following equations, for the critical interference, contact area, and load, are all independent of the hardness, which the current work shows not to be constant with respect to $S_y$. This is a notable improvement compared to previous elasto-plastic contact models [4–6]. The derivation is given in Appendix B, resulting in

$$\omega_c=\left(\frac{\pi\cdot C\cdot S_y}{2E'}\right)^2 R \tag{1}$$

where $C$ is derived in the Appendix to be

$$C=1.295\exp(0.736\nu) \tag{2}$$

The Poisson's ratio, $\nu$, to be used in Eq. (2) is that of the material which yields first. For $\nu=0.32$, as is used in this work, Eq. (2) results in $C=1.639$.

The critical load, $P_c$, is then calculated from the critical interference, $\omega_c$, by substituting Eq. (1) into Eq. (*A*2). The resulting critical contact force at initial yielding is thus

$$P_c=\frac{4}{3}\left(\frac{R}{E'}\right)^2\left(\frac{C}{2}\pi\cdot S_y\right)^3 \tag{3}$$

Similarly, the critical contact area is calculated from Eq. (*A*1) and is given by

$$A_c=\pi^3\left(\frac{CS_yR}{2E'}\right)^2 \tag{4}$$

These critical values predict analytically the onset of plasticity. These values are, therefore, chosen to normalize the results of all the models. The normalized parameters are

$$\omega^*=\omega/\omega_c \tag{5}$$

$$P^*=P/P_c \tag{6}$$

$$A^*=A/A_c \tag{7}$$

Normalizing the Hertzian contact area [Eq. (*A*1)] and force [Eq. (*A*2)], and the AF contact area [Eq. (*A*5)] and force [Eq. (*A*6)], by the critical values given in Eqs. (3) and (4), results in the following simplified expressions:

$$A_E^*=\omega^* \tag{8}$$

$$P_E^*=(\omega^*)^{3/2} \tag{9}$$

$$A_{AF}^*=2\omega^* \tag{10}$$

$$P_{AF}^*=\frac{3\mathrm{H}}{CS_y}\omega^* \tag{11}$$

## Finite Element Model

To improve upon the efficiency of computation, an axisymmetric 2-D model is used. The present study utilizes the commercial program ANSYS™, while ABAQUS™ produces the same results. Kogut and Etsion [4] also use ANSYS™. However, the mesh (see Fig. 2) in the current analysis is orders of magnitude more refined, as necessitated by mesh convergence [26]. The nodes at the base of the sphere are fixed in all directions. This boundary condition may be valid for the modeling of asperity contacts for two reasons: (1) The asperities are actually connected to a much larger bulk material at the base and will be significantly restrained there, and (2) since the high stress region occurs near the contact, the boundary condition at the base of the hemisphere will not greatly effect the solution because of Saint Venant's principle. The change in results between the said boundary conditions and one in which the nodes along axis $x$ are allowed to translate radially have shown only marginal difference (less than 3% difference in area, and less than 1% in load). While these boundary conditions may

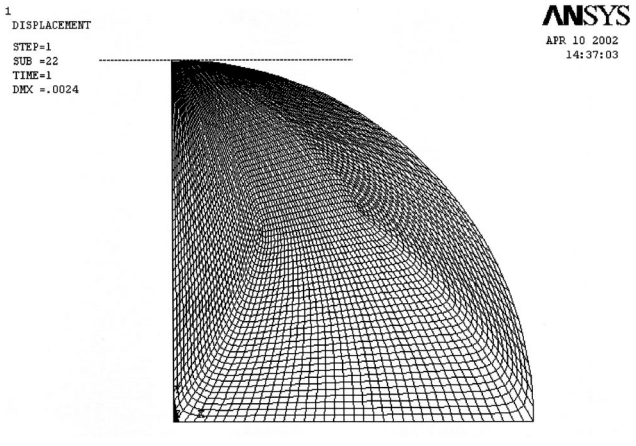


**Fig. 2 Finite element mesh of a sphere generated by ANSYS™**

not represent all possible loading scenarios, the conditions as stated are consistent with other models to facilitate an equitable comparison.

The contact region is meshed by 100 contact elements. The meshed contact area is also controlled to ensure that at least 30 contact elements are in contact for each applied interference (i.e., maximum contact radius error of 3.3%). These are in essence very stiff springs attached between surface nodes, and they activate only when penetration onset into the rigid flat is detected. It is important to assign a large value of stiffness for these contact elements so that negligible penetration occurs between the surfaces. However, using too high of a stiffness can result in convergence problems. This work uses a stiffness that is approximately the elastic modulus multiplied by a characteristic length (approximately the contact radius of the problem). In addition, if the penetration is greater than a defined value (tolerance), the Lagrangian multiplier method is used. This ensures that the penetration of the converged solution is less than the assigned tolerance. The tolerance of the current work is set to 1% of the element width. The contact elements thus apply forces to the nodes of the elements that are in contact.

The model refines the element mesh near the region of contact to allow the hemisphere's curvature to be captured and accurately simulated during deformation. The model uses quadrilateral, four node elements to mesh the hemisphere, but the results have also been confirmed to yield identical results using a mesh of eight node elements. The resulting ANSYS™ mesh is presented in Fig. 2, where ABAQUS™ produces a similar mesh. The quarter-circle mesh represents the axisymmetric hemispherical body, and the straight line represents the rigid plane.

The contact force acting on the hemisphere is found from the reaction forces on the hemisphere base nodes that retain the desired interference. The radius of the contact area is determined by finding the edge of the contact, or the location of the last activated contact element.

In order to validate the model, mesh convergence must be satisfied. The mesh density was iteratively increased by a factor of 2 until the contact force and contact area differed by less than 1% between iterations. The resulting mesh consists of at least 11,101 elements, since the number of meshed elements will vary with the expected region of contact. The stiffness of the contact elements was also increased by an order of magnitude in successive iterations until the contact force solution differed by no more than 1% between successive iterations.

In addition to mesh convergence, the model also compares well with the Hertz elastic solution at interferences below the critical interference. The contact force of the model differs from the Hertzian solution by no more than 2%. The contact radius differs by a maximum of 8.1%, but the average error is only 4.4%. When the contact areas are calculated from the radii, the maximum error increases to 17%. The smaller error in the contact force is attributed to overall force balance (static equilibrium) enforced by the FEM packages. However, the contact radius is obtained from a discrete mesh (which has a finite resolution). Moreover, the magnitude of the contact element stiffness also has some effect upon such radii, although not on the overall force balance. Generally, though, the differences are small enough that the FEM solution practically conforms to the Hertzian solution at interferences below critical (and even slightly above).

There are two ways to simulate the contact problem. The first applies a force to the rigid body and then computes the resulting displacement. The second applies a displacement and then computes the resulting contact force. In both methods, the displacement, stress, and strain in the elastic body can be determined, as well as the contact pressure. In this model the latter approach is used, where the base nodes of the hemisphere are displaced a distance or interference, $\omega$, approaching the rigid flat surface. The radial displacements of the base nodes are restricted. This method is used because the resulting solution converges more rapidly than the former.

The contact problem and the elasto-plastic material property make the analysis highly nonlinear and difficult to converge. An iterative scheme is used to solve for the solution, and many load steps are used to enhance solution convergence. Initially, a small interference is set of the total interference and then it is incremented after the load step converges. ANSYS™ internally controls the load stepping to obtain a converged solution by using the bisection method. This continues until a converged solution is found for the desired interference.

## Numerical Results and Discussion

The results of the described finite element hemisphere model are presented for a variety of interferences. While the elastic modulus and Poisson's ratio are held constant at 200 GPa and 0.32, respectively, five different material yield strengths are modeled. These are designated Mat.1 through Mat.5 corresponding to their yield strengths which are 0.210, 0.5608, 0.9115, 1.2653, and 1.619 GPa. The yield strengths cover a typical range of steel materials used in engineering [27]. The generated numerical data for five steel materials is given in Table 1. The results have also been confirmed for a larger range of material properties (other than steel) in Quicksall et al. [28]. Once the mesh is generated, computation takes from 10 min for small interferences to several hours for large interferences on a 2.5 GHz PC.

The dimensionless contact area is normalized by the Hertz solution [Eq. (8)] and plotted as functions of $\omega^*$ in Fig. 3. The data is presented on a log scale to capture the entire range of interferences. While $\omega^* < 1.9$ the finite element model agrees well with the Hertz solution ($A^*/\omega^* = 1$). This is likely because the plastic deformations are still relatively small such that the Hertz solution is not dramatically affected. As the sphere begins to plastically deform below the surface, the sphere weakens and thus does not retain its shape as well as if it were perfectly elastic throughout. Thus the area of contact eventually becomes larger in the elasto-plastic case than in the perfectly elastic case. The FEM model values for the dimensionless contact area continue to increase with interference even past Abbot and Firestone's fully plastic (AF) model [9] at $A^*/\omega^* = 2$. Since the AF model is based on the truncation of the contacting geometries, it does not model the actual deformation of the hemisphere. It seems reasonable, then, that the FEM solution for contact area could continue past the AF model.

Overall though, the FEM predicted contact area generally follows the Hertz elastic solution near the critical interference and then increases past the AF model as the interference increases. Later in this work, this trend will be followed by empirical formulations fitted to the data. The FEM results also indicate a material dependence of the normalized contact area. Since the con-

**Table 1 Tabulated finite element results (radius=1 $\mu$m, $E$ =200 GPa, $\nu$=0.32)**

(E=200 GPa, ν=0.32)

| MATERIAL | ω* | A* | P* |
|---|---|---|---|
| 1 | 101.91 | 1.774E+02 | 4.597E+02 |
| $S_y$=0.210 GPa | 135.88 | 2.522E+02 | 6.452E+02 |
| | 169.85 | 3.181E+02 | 8.376E+02 |
| | 203.82 | 4.017E+02 | 1.034E+03 |
| | 237.79 | 4.781E+02 | 1.235E+03 |
| | 271.76 | 5.589E+02 | 1.434E+03 |
| | 305.72 | 6.313E+02 | 1.642E+03 |
| | 339.69 | 7.105E+02 | 1.853E+03 |
| | 373.66 | 7.884E+02 | 2.048E+03 |
| | 407.63 | 8.766E+02 | 2.272E+03 |
| | 441.60 | 9.562E+02 | 2.471E+03 |
| | 475.57 | 1.037E+03 | 2.674E+03 |
| | 509.54 | 1.109E+03 | 2.889E+03 |
| 2 | 23.82 | 3.382E+01 | 7.815E+01 |
| $S_y$=0.5608 GPa | 47.64 | 7.793E+01 | 1.848E+02 |
| | 71.46 | 1.242E+02 | 3.034E+02 |
| | 95.28 | 1.751E+02 | 4.253E+02 |
| | 119.10 | 2.249E+02 | 5.453E+02 |
| | 142.93 | 2.768E+02 | 6.756E+02 |
| | 190.57 | 3.810E+02 | 9.402E+02 |
| | 238.21 | 4.914E+02 | 1.204E+03 |
| | 476.42 | 1.065E+03 | 2.517E+03 |
| 3 | 0.90 | 9.177E-01 | 8.585E-01 |
| $S_y$=0.9115 GPa | 2.25 | 2.419E+00 | 3.308E+00 |
| | 4.51 | 5.135E+00 | 8.782E+00 |
| | 6.76 | 7.999E+00 | 1.525E+01 |
| | 13.52 | 1.823E+01 | 3.811E+01 |
| | 18.03 | 2.592E+01 | 5.510E+01 |
| | 27.05 | 4.067E+01 | 9.219E+01 |
| | 36.06 | 5.776E+01 | 1.320E+02 |
| | 45.08 | 7.577E+01 | 1.699E+02 |
| | 54.09 | 9.258E+01 | 2.128E+02 |
| | 72.12 | 1.282E+02 | 2.998E+02 |
| | 90.15 | 1.662E+02 | 3.918E+02 |
| | 135.23 | 2.636E+02 | 6.234E+02 |
| | 180.31 | 3.644E+02 | 8.531E+02 |
| | 380.61 | 7.804E+02 | 1.747E+03 |

| MATERIAL | ω* | A* | P* |
|---|---|---|---|
| 4 | 0.47 | 5.468E-01 | 3.139E-01 |
| $S_y$=1.2653 GPa | 1.17 | 1.255E+00 | 1.267E+00 |
| | 2.34 | 2.472E+00 | 3.514E+00 |
| | 3.51 | 3.861E+00 | 6.236E+00 |
| | 4.68 | 5.308E+00 | 9.282E+00 |
| | 5.85 | 6.893E+00 | 1.259E+01 |
| | 7.02 | 8.582E+00 | 1.612E+01 |
| | 8.19 | 1.034E+01 | 1.977E+01 |
| | 9.36 | 1.210E+01 | 2.360E+01 |
| | 11.70 | 1.564E+01 | 3.188E+01 |
| | 14.04 | 1.923E+01 | 4.019E+01 |
| | 16.72 | 2.720E+01 | 5.806E+01 |
| | 23.39 | 3.513E+01 | 7.718E+01 |
| | 26.07 | 4.354E+01 | 9.712E+01 |
| | 37.43 | 6.062E+01 | 1.387E+02 |
| | 46.79 | 7.629E+01 | 1.822E+02 |
| | 93.58 | 1.742E+02 | 4.006E+02 |
| | 140.37 | 2.802E+02 | 6.322E+02 |
| | 187.16 | 3.821E+02 | 8.505E+02 |
| 5 | 0.29 | 3.133E-01 | 1.505E-01 |
| $S_y$=1.619 GPa | 0.43 | 4.766E-01 | 2.790E-01 |
| | 0.57 | 6.270E-01 | 4.324E-01 |
| | 0.71 | 7.691E-01 | 6.053E-01 |
| | 1.43 | 1.464E+00 | 1.720E+00 |
| | 2.14 | 2.243E+00 | 3.111E+00 |
| | 2.86 | 3.024E+00 | 4.695E+00 |
| | 3.57 | 3.923E+00 | 6.413E+00 |
| | 4.29 | 4.856E+00 | 8.263E+00 |
| | 5.00 | 5.844E+00 | 1.021E+01 |
| | 5.72 | 6.778E+00 | 1.225E+01 |
| | 6.43 | 7.781E+00 | 1.436E+01 |
| | 7.14 | 8.995E+00 | 1.654E+01 |
| | 7.86 | 9.999E+00 | 1.879E+01 |
| | 8.57 | 1.106E+01 | 2.111E+01 |
| | 9.29 | 1.217E+01 | 2.348E+01 |
| | 10.00 | 1.316E+01 | 2.593E+01 |
| | 11.43 | 1.545E+01 | 3.089E+01 |
| | 14.29 | 1.996E+01 | 4.138E+01 |
| | 17.15 | 2.491E+01 | 5.228E+01 |
| | 20.00 | 3.021E+01 | 6.367E+01 |
| | 24.29 | 3.743E+01 | 8.122E+01 |
| | 28.58 | 4.526E+01 | 9.944E+01 |
| | 31.43 | 5.118E+01 | 1.119E+02 |
| | 34.29 | 5.655E+01 | 1.246E+02 |
| | 40.01 | 6.711E+01 | 1.502E+02 |
| | 48.58 | 8.402E+01 | 1.861E+02 |
| | 54.29 | 9.648E+01 | 2.126E+02 |
| | 62.87 | 1.138E+02 | 2.519E+02 |
| | 68.58 | 1.257E+02 | 2.785E+02 |
| | 80.01 | 1.521E+02 | 3.321E+02 |
| | 100.02 | 1.959E+02 | 4.228E+02 |
| | 114.30 | 2.257E+02 | 4.923E+02 |
| | 171.46 | 3.556E+02 | 7.458E+02 |
| | 228.61 | 4.846E+02 | 9.795E+02 |

tact area is calculated by counting the number of elements in contact, and there are only a finite number of such elements, there is an inherent error in the data. The scatter in the data can be attributed mostly to this, and to the fact that the FEM is yet a discrete formulation.

For the contact area, all the models follow the same general trend, but they differ in magnitude. The ZMC model follows the Hertz elastic solution at low and moderate interferences, but abruptly migrates to the AF model before the current model and the KE model. The KE model and the current empirical model also agree fairly well on average, except at large interferences. The KE model clearly shows a slight discontinuity at $\omega^*=6$ and then terminates at $\omega^*=110$. The KE model does not connect with the Hertz elastic solution at the critical interference depth. Also, the nondimensional KE model is material independent such that its contact area falls between the data of materials 1 and 5 of this work.

The dimensionless contact force is normalized by the Hertz solution [Eq. (9)] and plotted as a function of $\omega^*$ in Fig. 4. This plot uses a log scale to capture the entire range of interferences. The normalized contact force $[P^*/(\omega^*)^{3/2}]$ calculated from the current model follows precisely the Hertz elastic solution $[P^*/(\omega^*)^{3/2}=1]$ at small interferences. With increasing interference the current model eventually increases toward the AF model [9]. It is interesting to note that the AF model predicts higher loads at small interferences than the Hertzian solution, but eventually crosses over to become the lesser of the two. This is because the AF model assumes a constant pressure distribution, which is equal to the hardness, while the average pressure of the Hertzian solution is initially lower than the hardness. At higher interferences, the FEM data displays a material dependent behavior.

The nondimensional contact force trends of all the models are similar; however, the ZMC again crosses to the AF model prematurely. At low interferences, the KE and ZMC models predict a contact force that is greater than the elastic model. This cannot be the case, as the yield strength of the material limits the stiffness of the hemisphere. Again the KE model shows a discontinuity at $\omega^*=6$ and then terminates at $\omega^*=110$. Generally the KE model and the current FEM results are very similar. At about $\omega^*=50$ the KE model crosses over the current model and continues to overestimate the contact force until $\omega^*=110$. The KE and ZMC models also fail to capture the material dependence effects at large interferences.

The average contact pressure to yield strength ratio, $P/(AS_y)$, is calculated from the data and plotted in Fig. 5, alongside the Hertz contact solution. The Firestone and Abbott [9] fully plastic (AF) model is represented by the horizontal line at $P/(AS_y)=3$. The average contact pressure should approach the hardness of the material as the contact becomes fully plastic. It is widely accepted that the hardness is approximated by $3\cdot S_y$ [11]. It becomes evident in this plot that this is not always the case. From the data it

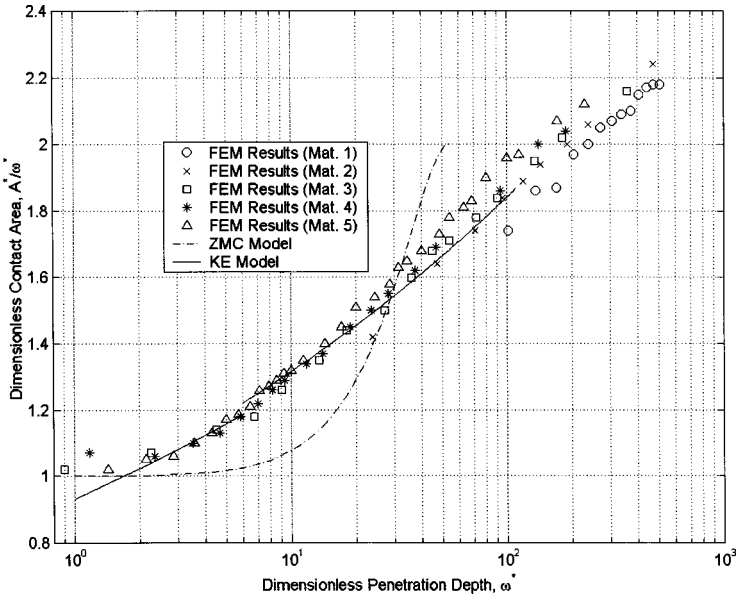


**Fig. 3 FEM predicted contact area**

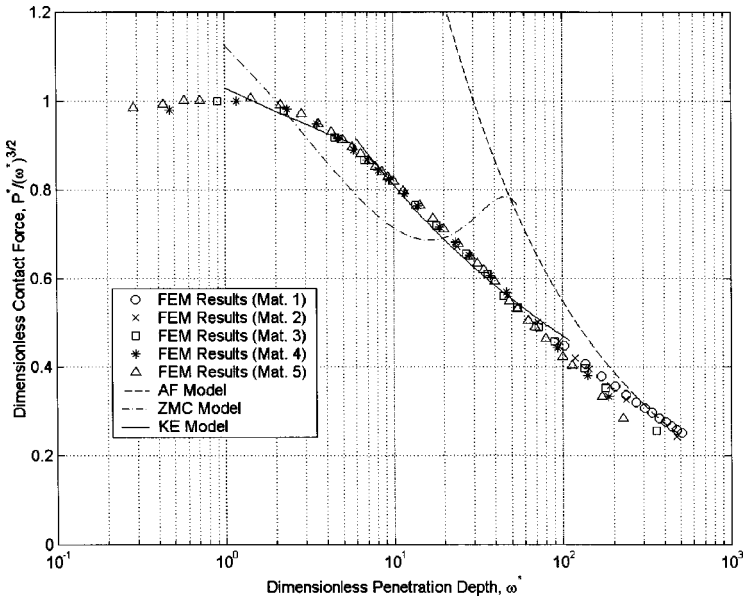


**Fig. 4 FEM predicted contact force**

seems that hardness is not a constant material property. The cause of this trend will be discussed later in greater detail. The work by Mesarovic and Fleck [15] also confirms this trend, but does not address the trend theoretically.

## Empirical Formulation

General empirical approximations of the FEM data are desired for use at any deflection and for any set of material properties. This will help designers in a variety of single contact problems, and it will be readily incorporated into statistical models to model rough surfaces.

As mentioned previously, the FEM solution for the area of contact continues past the AF model with increasing interference. Hence, the leading coefficient in Eq. (10) is allowed to vary when equations are fitted to the FEM data. This is reasonable, since the AF model is not an exact solution (it is based on a truncation assumption). Here a power function is used in place of this leading coefficient and is fit to the numerical data. Figures 3–5 show that there are two distinct regions in the FEM data; thus a piecewise formulation is used to fit the data. At small interferences the Hertz solution is assumed and at large interferences the power function is fit to the FEM data, resulting in the following:

For $0 \leqslant \omega^* \leqslant \omega_t^*$

$$A_F^* = \omega^* \tag{12}$$

and for $\omega_t^* \leqslant \omega^*$

$$A_F^* = \omega^* \left( \frac{\omega^*}{\omega_t^*} \right)^B \tag{13}$$

where

$$B = 0.14 \exp(23 e_y) \tag{14}$$

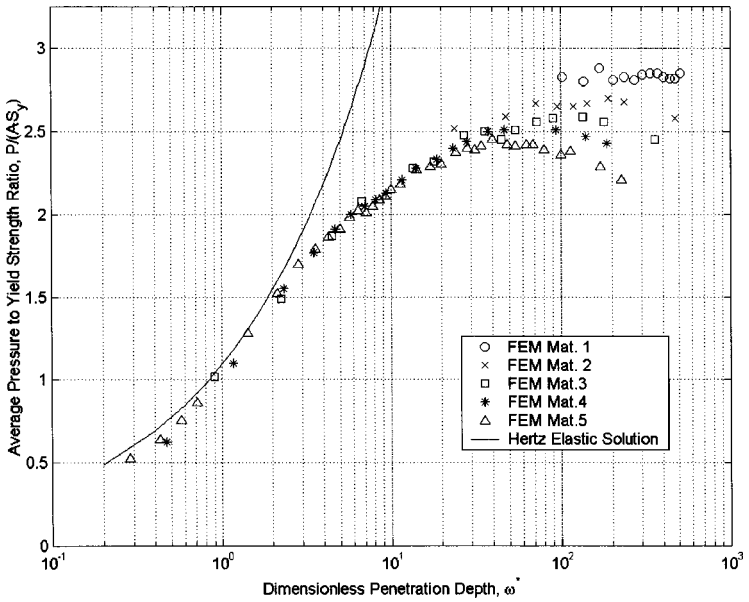


**Fig. 5 Average contact pressure to yield strength ratio**

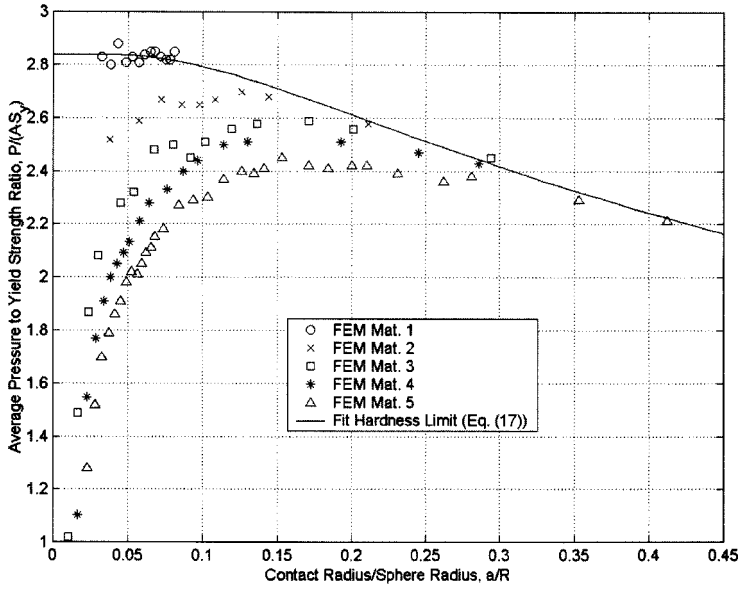


**Fig. 6 Average contact pressure to yield strength ratio**

$$e_y = \frac{S_y}{E'} \tag{15}$$

$$\omega_t^* = 1.9 \tag{16}$$

The value $\omega_t^*$ represents the transition point from elastically dominant behavior to elasto-plastic behavior. The formulation follows the Hertzian solution [Eq. (12)] for $\omega^* < 1.9$. Then it transitions to the elasto-plastic case and eventually continues past the AF model for high values of $\omega^*$. Equation (13) is also somewhat dependent on the material properties, according to the definition in Eqs. (14) and (15). Statistically, Eq. (13) differs from the FEM data for all five materials by an average of 1.3% and a maximum of 4.3%. An equation of the same form as the ZMC model fitted to the FEM data results in an average error of 43.2%. Notably, Eqs. (12) and (13) are continuous at $\omega_t^*$.

In order to formulate a fit for the FEM contact force, the material-dependent trend at high interferences shown in Fig. 4 is modeled. To assist in this model, a plot of $P/(AS_y)$ as a function of $a/R$ in Fig. 6 reveals the cause of the material dependency. In this plot a limit appears to emerge for the fully plastic average pressure, commonly referred to as the hardness. Here the hardness appears to change as a function of $a/R$, or with the evolving geometry of contact. The trend may be explained by the progression schematically shown in Fig. 7. As the interference increases and the contact geometry changes, the limiting average pressure to yield strength ratio, $H_G/S_y$, must change from Tabor's predicted value of 3 to a theoretical value of 1 when $a=R$. The contact region when $a=R$ is essentially the case of a deformable blunt rod in contact with a rigid flat whose $H_G/S_y$ value is theoretically one. A Weibull function fitted to the limiting values of $H_G$ results in

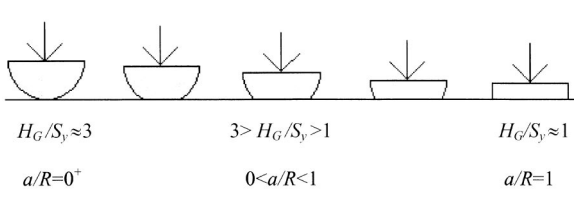


**Fig. 7 Progression of change in hardness with deformed geometry**

$$\frac{H_G}{S_y} = 2.84\left[1 - \exp\left(-0.82\left(\frac{a}{R}\right)^{-0.7}\right)\right] \tag{17}$$

This formulation is plotted alongside the data in Fig. 6. Interestingly, as $a/R$ approaches zero, the limiting value of $H_G/S_y = 2.84$ agrees almost precisely with the theoretical value of 2.83 (Williams [[29], p. 109]). Equation (17) is only valid for the range of fitted data (or $0 < a/R \leq 0.412$). Caution should thus be taken when using this function outside this range. This range is acceptable for many applications, particularly tribological applications where deformations above this range are either unlikely or unacceptable. From the relation $A = \pi \cdot a^2$, $a$ is solved for and normalized by $R$. Then $A_c \cdot A_F^*$ is substituted for $A$. Equation (13) is then substituted for $A_F^*$, andEq. (4) for $A_c$, thus yielding

$$\frac{a}{R} = \frac{\sqrt{A_c \cdot A_F^*}}{\sqrt{\pi}R} = \sqrt{\frac{\pi^3 (CS_y R)^2 \omega^* (\omega^*/\omega_t^*)^B}{4\pi (RE')^2}} = \frac{\pi C e_y}{2}\left[\omega^*\left(\frac{\omega^*}{\omega_t^*}\right)^B\right]^{1/2} \tag{18}$$

This substitution is valid only when $\omega^* \geq \omega_t^*$. Equation (18) can then be substituted into Eq. (17) so it may then be rewritten as a function of $\omega^*$ as follows:

$$\frac{H_G}{S_y} = 2.84\left[1 - \exp\left(-0.82\left(\frac{\pi C e_y}{2}\sqrt{\omega^*}\left(\frac{\omega^*}{\omega_t^*}\right)^{B/2}\right)^{-0.7}\right)\right] \tag{19}$$

This results in a formulation for $H_G$ as a function of the material properties, $E$, $S_y$, and $\nu$ (not just upon $S_y$ as suggested by Tabor [11]).

To formulate an approximation of the contact force as predicted by the FEM results, the AF model for contact force must first be corrected by way of substituting Eq. (17) or (19) into Eq. (11), letting $H_G$ replace $H$, and by allowing the AF contact area to deviate from Eq. (10) [see reasoning for Eq. (17)]. This results in an equation for a corrected fully plastic model. Once again a piecewise solution is fit to the FEM data. At small interferences, the Hertz solution is assumed. The resulting piecewise equation fit to the FEM data is given as follows:

For $0 \leq \omega^* \leq \omega_t^*$

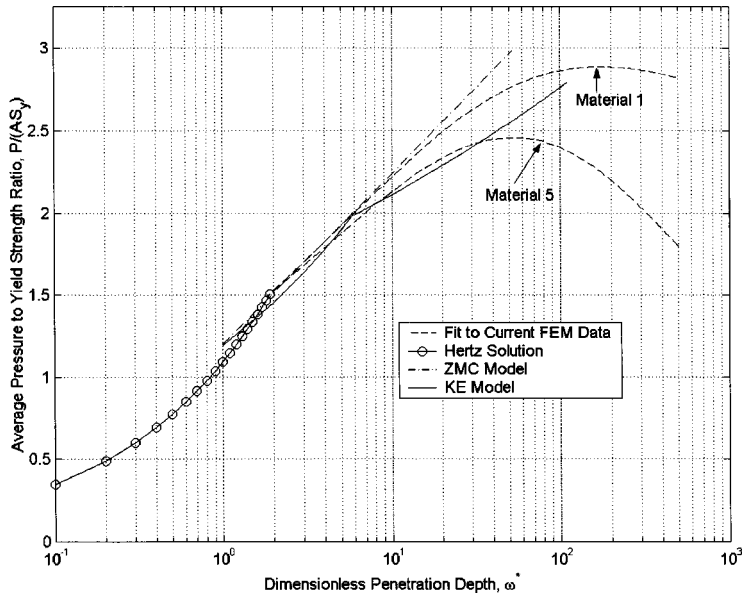


**Fig. 8 Predicted average pressure to yield strength ratio for various models**

$$P_F^* = (\omega^*)^{3/2} \tag{20}$$

and for $\omega_t^* \leq \omega^*$

$$P_F^* = \left[\exp\left(-\frac{1}{4}(\omega^*)^{5/12}\right)\right](\omega^*)^{3/2} + \frac{4H_G}{CS_y}\left[1-\exp\left(-\frac{1}{25}(\omega^*)^{5/9}\right)\right]\omega^* \tag{21}$$

where $\omega_t^* = 1.9$. This formulation approaches asymptotically the Hertz elastic model at small interferences, and approaches and continues past the AF model at large interferences. Statistically this formulation differs from the FEM data for all five materials by an average error of 0.94% and a maximum of 3.5% when Eq. (19) is used for $H_G$.

The average pressure to yield strength ratio, $P/(AS_y)$, can now be modeled by combining Eqs. (12)–(16) and Eqs. (20) and (21). Since these equations are normalized by their critical values, the resulting formulation for the average pressure is

$$\frac{P}{AS_y} = \frac{2}{3}C\frac{P_F^*}{A_F^*} \tag{22}$$

This ratio is shown in Fig. 8 (only the weakest and strongest materials are plotted for clarity). The largest differences between the ZMC and KE models and the current FEM model then appear. It is apparent that the KE and ZMC models do not account for material dependence in the limiting average pressure to yield strength ratio, $H_G/Sy$. Both the ZMC and KE models are monotonically increasing and truncated at some point that traditionally is considered to be the ''hardness.'' The ZMC and KE models both estimate the average pressure in the transition from the elastic to the elasto-plastic regime fairly well. It is also apparent that these models do not intersect with the Hertzian solution at $P/(AS_y) = 2 \cdot C/3$. The discontinuity in the slope in the KE model at a value of 6 and in the current model at a value of 1.9 is also clearly evident [see Eqs. (*A*8) and (*A*9) and Eqs. (12)–(21)].

## Comparison with Experimental Results

Johnson [25] performed experiments on the elasto-plastic contact of copper cylinders and spheres. During one experiment, he tested the contact of a copper sphere and a comparatively rigid steel surface. These test conditions are comparable to the sphere against a rigid flat case modeled in this work. For the highest load tested, the contact has a nearly uniform pressure distribution, thus suggesting it is in the fully plastic regime. At this load, the $a/R$ ratio is given as 0.204 and the average pressure as $2.59 \cdot S_y$. Interestingly, the predicted geometric hardness limit or average pressure for the same $a/R$ using Eq. (17) is $2.61 \cdot S_y$. In comparison, the KE model, which assumes the AF model at this interference, predicts an average pressure of $2.8 \cdot S_y$.

Johnson provides the contact radius and load in his results, which can also be compared with the predictions of the current formulations [Eqs. (12)–(21)] and those of the KE model [Eqs. (*A*8) and (*A*9)]. Table 2 presents this comparison. The material properties provided by Johnson were used when available; otherwise values from [27] were used. All material properties are given in Table 2. Since Johnson does not provide the interference at each load, the predicted pressure is calculated from the experi-

**Table 2 Comparison of experimental [25] and numerical results**

| $P^*$ (EXPERIMENTAL) | $A^*$ (EXPERIMENTAL) | $P^*$ (CURRENT) | % *DIFF.* | $P^*$ (KE) | % *DIFF.* |
|---|---|---|---|---|---|
| 360.1 | 159.4 | 404.3 | 10.9 | 400.9 | 10.2 |
| 1230.5 | 527.4 | 1306.3 | 5.8 | 1331.9[&] | 7.6 |
| 2401.0 | 1042.8 | 2442.6 | 1.7 | 2633.3[&] | 8.8 |
| Material Properties, Copper: $Sy$=265.5 kPa $E$=115 GPa $\nu$=0.34 Steel: $E$=200 GPa $\nu$=0.33 | | | | | |

[&]The KE model assumes the results of Abbott and Firestone [9] for fully plastic contact.

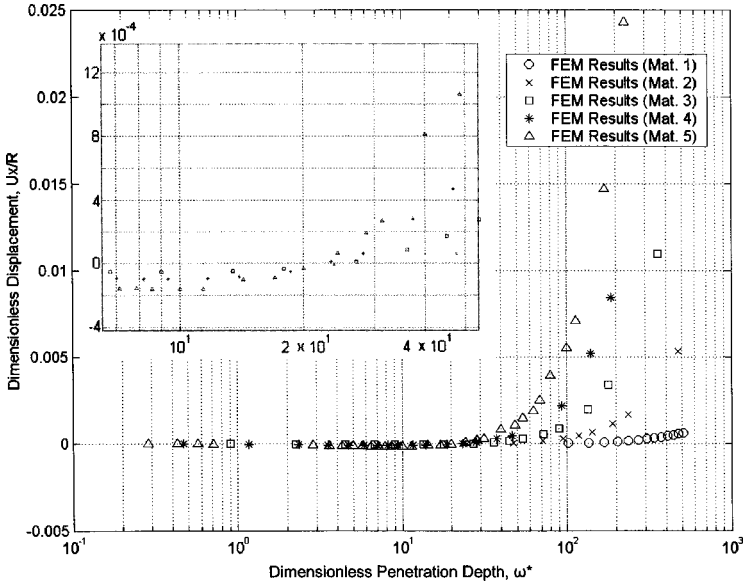


**Fig. 9 Displacement at edge of contact area plotted as a function of penetration depth**

mental contact area using the current formulations and the KE model. Both numerical models compare well with the experimental results and differ by a maximum of just over 10%. However, overall the current model proves to be a more accurate model. In fact, at the largest load the difference is merely 1.7%. These results also indicate that there is a definite need for formulations which can accurately capture elasto-plastic hemispherical contact at large interferences. The experimental results also show again that the hardness or the fully plastic average pressure varies with deformation and is not constant at $2.8 \cdot S_y$ or $3 \cdot S_y$ [4,9].

## Evolution of Deformation

As long as the deformations are purely elastic, i.e., below the critical interferences, the entire hemisphere will abide to 3D Hooke's law. Conforming to Poisson's effect, the material volume should compress with a compressive contact pressure [as shown schematically in Fig. 1(*b*)]. To investigate this phenomenon Fig. 9 shows the radial deformation of the last contact point between the deformed hemisphere and the rigid flat as extracted from the FEM postprocessing data. Indeed at relatively small values of $\omega^*$ there seems to be a shrinkage in volume (even though that some plastic deformation has already taken place, but overall the elastic deformation of the entire hemisphere dominates). At values below an approximate value of $\omega^* = 22$, the radial displacements are all negative, very small, and are generally strength independent (see inset). In plasticity, however, volume is conserved. As the deformation increases, the yielded material flows plastically and is incompressible, making Poisson's ratio effectively equal to 0.5 [30]. The FEM results find that beyond $\omega^* = 22$ (approximately), the radial deformation of the last contact point displaces positively, i.e., the schematics of the deformation follows the geometry depicted in Fig. 1(*c*). The positive displacement becomes material dependent, which increases with material strength.

## Stress Distribution and Evolution

Initially, at small interferences, the sphere will deform only elastically. While in the elastic regime, the maximum von Mises stress will always occur beneath the contact surface and within the bulk material. Eventually, as the interference increases and the stresses increase, yielding will initiate at the point of maximum von Mises stress.

At interferences just above the critical, the plastically deformed region is small and confined below the surface by a sizeable region of elastic material [see Fig. 10(*a*)]. It should be noted that because of plotting resolution the region of plastic deformation is smaller then the highest stress region shown in each plot. For instance, the highest stress region in Fig. 10(*b*) has a von Mises stress range between 1.444 and 1.624 GPa, and thus not the entire region in this stress range is at the yield stress of 1.619 GPa. With increasing interference, the plastic region expands until it reaches the surface of the sphere [Figs. 10(*b*) and 10(*c*)]. From close inspection of postprocessing data, according to the current model, the interference at which the plastically deformed region first reaches the surface is approximately when $\omega_s^* = 9.6$, for material 5 (this differs from the value $\omega_s^* = 6$ as reported by Kogut and Etsion [4]). The value of $\omega_s^*$ also varies slightly with the material yield strength and the deformed contact geometry for the same reason that the average pressure or hardness varies with strength.

Repeated FEM analyses were performed to search for the interferences of two important cases: (1) when plastic deformation first reaches the contacting surface at the far right end point, and (2) when the contact surface first becomes entirely (fully) plastic. Table 3 gives these results. To pinpoint precisely these values, much more arduous searches are needed. The search performed here, albeit intensive, was not exhaustive and, therefore, the values given here contain some uncertainty (given as the resolution in Table 3). Searches were done on the stronger materials excluding materials 1 and 2, which have the slowest convergence rates.

After plastic deformation has reached the surface, an elastic volume on the loaded tip of the sphere is still maintained [Fig. 10(*c*)] by the presence of hydrostatic stresses, which suppress yielding according to the von Mises criterion. Eventually this elastic region will turn plastic as the interference is increased. Figure 10(*d*) shows a state of stress just before the fully plastic state is reached on the contact surface. Although an exhaustive analysis of $\omega_{fp}^*$ is not performed here, this initial fully plastic interference seems to range between $\omega^* = 70$ and $\omega^* = 80$, depending on the material yield strength. This range of values is also close to the value of 68 as predicted by the KE model.

## Conclusions

This work presents a 2D axisymmetric finite element model of an elastic-perfectly plastic hemisphere in contact with a rigid flat surface. A comparison is also made with other existing models. The material is modeled as elastic-perfectly plastic, and yielding occurs according to the von Mises criterion. A concise form is

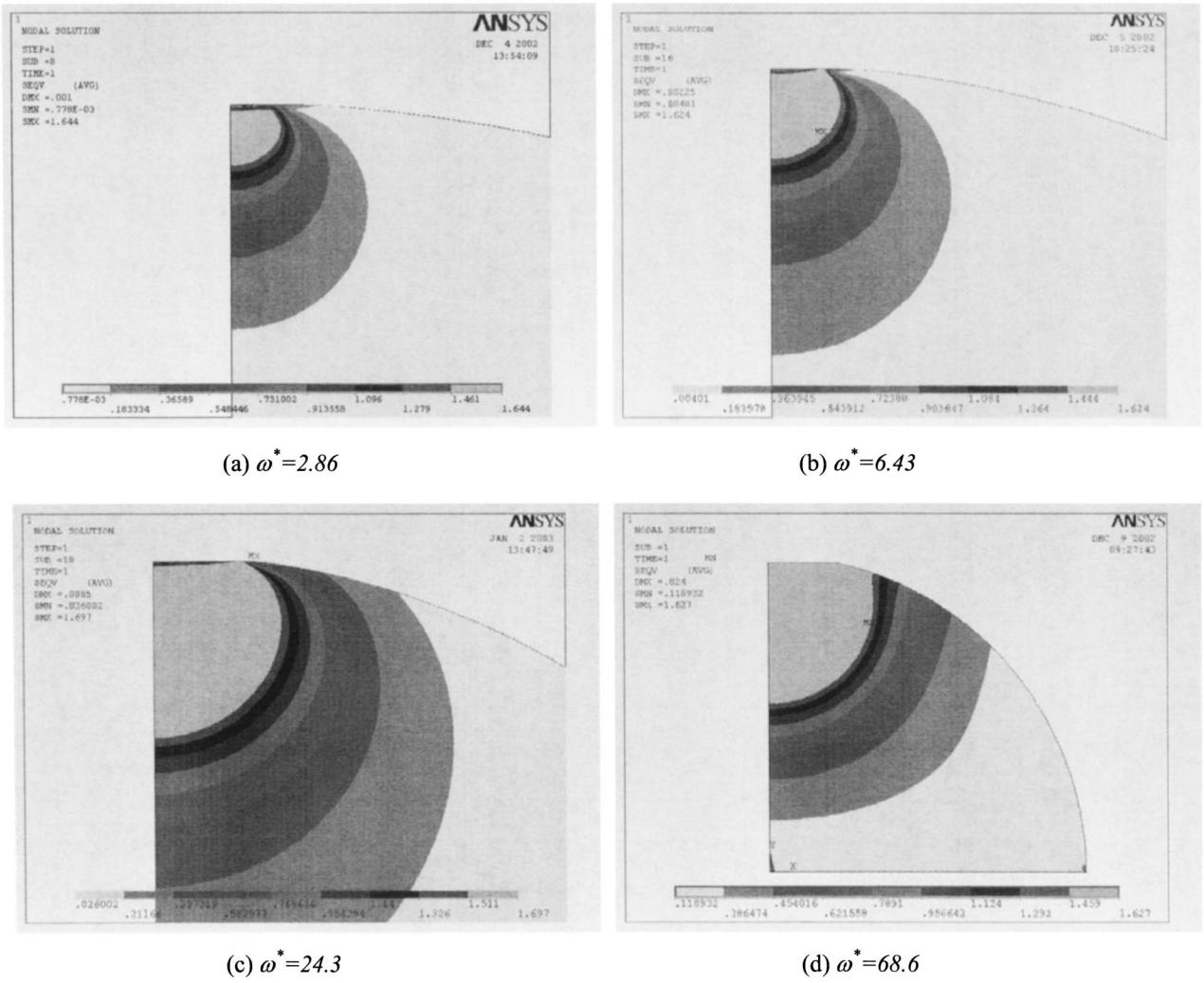


(a) $\omega^*=2.86$ (b) $\omega^*=6.43$

(c) $\omega^*=24.3$ (d) $\omega^*=68.6$

**Fig. 10 Stress plots from ANSYS™, showing the evolution of the stress distribution from (*a*) elasto-plastic (not yet plastic on surface) to (*d*) just before fully plastic**

presented for the critical interference at which plastic deformation initiates within the hemisphere. It is derived from the Hertzian solution and the von Mises yield criterion. An a priori definition of the hardness is not needed.

The resulting plots indicate that the FEM results for the contact area agree closely at small interferences with the trends of the Hertzian solution. While at large interferences the FEM predicts contact areas that surpass Abbot and Firestone's fully plastic model [9] (that is based upon truncation). The ZMC model is found to differ significantly from the FEM results, where the KE model (which is also based on FEM results) follows more closely, although still does not capture the varying hardness trend. An empirical formulation for the contact area is also fitted to the FEM data as a function of the material properties and interference.

The FEM results of the contact force predict a lower load carrying capacity than the AF model for most materials and values of $\omega^*$. This is because the AF model assumes that the average pressure distribution is simply the hardness, which is approximated by $3 \cdot S_y$. It is found, however, that the fully plastic average contact pressure or hardness is not constant as is widely accepted. Rather, the limiting value of the fully plastic average pressure varies with the deformed contact geometry, which in turn is coupled to the

**Table 3 FEM generated interferences for initial yield of the surface and the fully plastic regime**

| MATERIAL ($S_y/E$) | $\omega^*$ AT INITIAL SURFACE YIELD | RESOLUTION | $\omega^*$ AT INITIAL FULLY PLASTIC | RESOLUTION |
|---|---|---|---|---|
| 0.00456 | 7.89 | +/-1.13 | 81.13 | +/- 9.01 |
| 0.00633 | 9.36 | +/- 0.58 | 81.87 | +/- 11.70 |
| 0.00810 | 9.64 | +/- 0.36 | 74.23 | +/- 5.71 |

material yield strength. This is accounted for in an empirical formulation for the limiting average pressure to yield strength ratio, $H_G/S_y$. A formulation using $H_G/S_y$ is then fit to the FEM contact force data.

A comparison is also made with the experimental results provided by Johnson [25]. The current model compares very well, and predicts the sparse experimental results significantly better than the KE model, particularly in the fully plastic regime. The experimental results also show that the hardness trend at large deformation is a very real phenomenon that can affect practical engineering applications.

This work reveals large differences between approximate analytical models and other numerical solutions. More importantly, the contact area, force, and pressure are found to be particularly dependent upon the deformed geometry in all regimes and effectively dependent upon the material properties (e.g., strength) in the elasto-plastic and plastic regimes. The fit-them-all equations that solely depend upon deformation, which are found in previous works, are imprecise when compared to current FEM results. For example, the average contact pressure to yield strength ratio in all previous work is shown to increase monotonically with deformation, and is assumed to terminate (or truncate) at the hardness. In this work it is shown that such a truncation is not warranted. Particularly, it is shown that the truncation model of Abbott and Firestone [9] cannot be justified. This work discovered significant geometrical and material nonlinearities, and that the hardness depends not just upon strength but also upon the modulus of elasticity, Poisson's ratio, and most importantly upon the deformation itself (i.e., hardness is not a unique or fixed material property as indicated by Tabor [11], and assumed by others after him). The results are based on the finest and adaptive mesh yet (over 11,000 four- and eight-node elements for a single hemispherical asperity in contact with a rigid flat, and 100 contact elements) that is necessary for finite element convergence. The results were obtained by using ANSYS™ and then independently confirmed by using ABAQUS™. In the future it would be useful to investigate the effect of material strain hardening and tangential loading (sliding).


## Acknowledgments

The contribution of Dawei Shen of Georgia Tech in helping to construct the ANSYS™ FEM model is gratefully acknowledged. The contribution of Scott Shipley of Georgia Tech in confirming the results using ABAQUS™ software is also gratefully acknowledge.


## Nomenclature

- $A$ = area of contact
- $C$ = critical yield stress coefficient
- $E$ = elastic modulus
- $H$ = hardness
- $H_G$ = hardness geometric limit
- $K$ = hardness factor
- $P$ = contact force
- $R$ = radius of hemispherical asperity
- $S_y$ = yield strength
- $a$ = radius of the area of contact
- $e_y$ = uniaxial yield strain, $S_y/E$
- $k$ = mean contact pressure factor
- $p_o$ = maximum contact pressure
- $z$ = axis of symmetry for hemisphere
- $\omega$ = interference between hemisphere and surface
- $\nu$ = Poisson's ratio

**Subscripts**

- $E$ = elastic regime
- $F$ = fit to current FEM data
- $c$ = critical value at onset of plastic deformation
- $o$ = maximum
- $t$ = transitional value from elastic to elasto-plastic behavior

**Superscripts**

- $'$ = equivalent
- $*$ = dimensionless.

## Appendix A: Existing Hemispherical Contact Models

The Hertzian solution [2] provides closed-form expressions to the deformations and stresses of two spheres in a purely elastic contact. The two spheres may have different radii and different elastic properties. However, the closed-form solutions render an equivalent case where a single elastic sphere, having an equivalent elastic modulus, $E'$, and an equivalent radius, $R$, is in contact with a rigid flat [see Fig. 1, and Eqs. (*A*1)–(*A*4) that follow]. The interference, $\omega$, can be described as the distance the sphere is displaced normally into the rigid flat. The Hertz solution assumes that the interference is small enough such that the geometry does not change significantly. The solution also approximates the sphere surface as a parabolic curve with an equivalent radius of curvature at its tip. The resulting equations for contact radius and load from the Hertz solution are

$$A_E = \pi R \omega \tag{A1}$$

$$P_E = \frac{4}{3} E' \sqrt{R} (\omega)^{3/2} \tag{A2}$$

where

$$\frac{1}{E'} = \frac{1-\nu_1^2}{E_1} + \frac{1-\nu_2^2}{E_2} \tag{A3}$$

$$\frac{1}{R} = \frac{1}{R_1} + \frac{1}{R_2} \tag{A4}$$

and $E_1$, $\nu_1$, $R_1$ and $E_2$, $\nu_2$, $R_2$ are the elastic properties and radii of sphere 1 and 2, respectively.

Abbott and Firestone [9] stated that under fully plastic conditions the area of contact of an asperity pressed against a rigid flat can be approximately calculated by truncating the asperity tips as the rigid flat translates an interference, $\omega$. For a hemisphere, this approximated fully plastic area is given by

$$A_{AF} = 2\pi R \omega \tag{A5}$$

Using Eq. (*A*5) the contact load of the hemispherical asperity is simply the contact area multiplied by the average contact pressure, which in this case is the hardness, since the contact is assumed to be fully plastic. The approximated fully plastic contact force is thus

$$P_{AF} = 2\pi R \omega H \tag{A6}$$

From this point forward, Eqs. (*A*5) and (*A*6) will be referred to as the AF model. Greenwood and Tripp [10] also independently model fully plastic contact between hemispheres using a similar truncation method.

Chang et al. [5] (CEB model) approximated elasto-plastic contact by modeling a plastically deformed portion of a hemisphere using volume conservation. This CEB model assumes that (1) the hemisphere deformation is localized to near its tip, (2) the hemisphere behaves elastically below the critical interference, $\omega_c$, and fully plastically above that value, and (3) the volume of the plastically deformed hemisphere is conserved. Also, the critical interference used in the CEB model is given by

$$\omega_c = \left( \frac{\pi K H}{2E'} \right)^2 R \tag{A7}$$

where $K$ is the hardness factor given by $K = 0.454 + 0.41\nu$ and the hardness is assumed $H = 2.8 \cdot S_y$. While from an engineering perspective the corresponding values given by Eqs. (1) and (*A*7) are

very close, the CEB model is limited to this fixed relationship between the hardness and the yield strength. It should be noted that Eq. (1) is not limited by any such assumption. Likewise the CEB model contains a discontinuity at $\omega_c$.

Zhao et al. [6] devised an elasto-plastic (ZMC) model, which interpolates between the elastic and fully plastic (AF) models. The ZMC model divides the interference into three segments: (1) elastic (Hertz), (2) elasto-plastic (using a template), and (3) fully plastic (AF). A template function satisfies continuity of the function and its slope at the two transitions. The works [7,8] take semi-analytical approaches to the problem.

Kogut and Etsion [4] also performed a FEM analysis of the same case of an elastic-perfectly plastic sphere in contact with a rigid flat. Again in their analysis, the value of $H$ is set to be fixed at $2.8 \cdot S_y$. Notably, the slope of $P/(AS_y)$ is not zero (it still increases monotonically) at the point where full plasticity is assumed. Their work gives a very detailed analysis of the stress distribution in the contact region, and empirical expressions are provided for the contact area, the contact force, and the average contact pressure. The resulting equations have a discontinuous slope at $\omega^*=6$, and they describe the deformation only up to $\omega^*=110$, at which point full plasticity is assumed. These are given in a piecewise form:
For $1 \leqslant \omega^* \leqslant 6$

$$P^*_{KE} = 1.03(\omega^*)^{1.425}$$
$$A^*_{KE} = 0.93(\omega^*)^{1.136} \tag{A8}$$
$$\left(\frac{P}{AS_y}\right)_{KE} = 1.19(\omega^*)^{0.289}$$

For $6 \leqslant \omega^* \leqslant 110$

$$P^*_{KE} = 1.40(\omega^*)^{1.263}$$
$$A^*_{KE} = 0.94(\omega^*)^{1.146} \tag{A9}$$
$$\left(\frac{P}{AS_y}\right)_{KE} = 1.61(\omega^*)^{0.117}$$

These equations have a discontinuous slope at $\omega^*=6$, and they describe the deformation only up to $\omega^*=110$, at which point full plasticity and the AF model is assumed. At values $\omega^*<1$ the Hertz contact solution is assumed.

## Appendix B: Critical Interference

The Hertz solution results in the following equations for stress within the deformed sphere along the axis of revolution, $z$ (Johnson, [20]):

$$\sigma_1 = -p_o\left(1+\left(\frac{z}{a}\right)^2\right)^{-1} \tag{B1}$$

$$\sigma_{2,3} = p_o\left\{\left[2\left(1+\left(\frac{z}{a}\right)^2\right)\right]^{-1} - (1+\nu)\left[1-\frac{z}{a}\tan^{-1}\left(\frac{a}{z}\right)\right]\right\} \tag{B2}$$

where the origin of the $z$-axis lies at the point of initial contact between the hemisphere and the rigid flat, and $p_o$ is the maximum contact pressure.

The von Mises yield criterion is given as

$$S_y = \sqrt{\frac{1}{2}[(\sigma_1-\sigma_2)^2+(\sigma_2-\sigma_3)^2+(\sigma_3-\sigma_1)^2]} \tag{B3}$$

By substituting the principal stresses given in Eqs. (*B*1) and (*B*2) into Eq. (*B*3) and then simplifying, the following equation for the von Mises yield criterion is obtained:

$$\frac{S_y}{p_o} = \frac{3}{2}\left(1+\left(\frac{z}{a}\right)^2\right)^{-1} - (1+\nu)\left[1-\frac{z}{a}\tan^{-1}\left(\frac{a}{z}\right)\right] \tag{B4}$$

The resulting Eq. (*B*4), which must be positive, dictates where within the hemisphere initial yielding occurs. This is obtained by setting the derivative with respect to $z$ to zero. Hence,

$$\frac{d}{dz}\left(\frac{S_y}{p_o}\right) = -az[a^2(4+\nu)+(1+\nu)z^2] + (1+\nu)(a^2+z^2)^2\left[\tan^{-1}\left(\frac{a}{z}\right)\right] = 0 \tag{B5}$$

This equation is solved numerically for Poisson's ratios between 0.01 and 0.50 to find the locations, $z$, at initial yielding. These locations are then substituted in Eq. (*B*4) to find the applied maximum contact pressure to yield strength ratio, $p_{oc}/S_y$. This ratio, $p_{oc}/S_{y,}$ is referred to as the yield strength coefficient and designated by the symbol $C$. An empirical function is fitted to the final numerical data, which is given by

$$\frac{p_{oc}}{S_y} = C = 1.295\exp(0.736\nu) \tag{B6}$$

Equation (*B*6) differs from the numerical solution by an average of 1.2% and by no more than 3.1%.

The interference,$\omega$, is given as a function of $p_o$ by the Hertz elastic solution in Johnson [20] as

$$\omega = \left(\frac{\pi \cdot p_o}{2E'}\right)^2 R \tag{B7}$$

Thus, to find the critical interference, or the interference at the initial point of yielding, the maximum pressure when yielding first occurs, $p_{oc}$, is substituted into Eq. (*B*7) for $p_o$. This maximum pressure is the pressure given by the maximum contact to yield strength ratio given in Eq. (*B*6). The equation $p_{oc}=CS_y$ is substituted into Eq. (*B*7), resulting in Eq. (1).

A similar derivation is also given in Chang [31]. However, that derivation assumed a fixed value between strength and hardness, $S_y=0.35H$, which resulted in an equation for the hardness coefficient, $K=0.454+0.41\nu$. Such an assumption is not made in this work (see discussion on $H_G$ within).

## References


[1] Greenwood, J. A., and Williamson, J. B. P., 1966, "Contact of Nominally Flat Surfaces," Proc. R. Soc. London, Ser. A, **295**, pp. 300–319.
[2] Timoshenko, S., and Goodier, J. N., 1951, *Theory of Elasticity*, McGraw-Hill, New York.
[3] Green, I., 2002, "A Transient Dynamic Analysis of Mechanical Seals Including Asperity Contact and Face Deformation," Tribol. Trans., **45**(3), pp. 284–293.
[4] Kogut, L., and Etsion, I., 2002, "Elastic-Plastic Contact Analysis of a Sphere and a Rigid Flat," Trans. ASME, J. Appl. Mech., **69**(5), pp. 657–662.
[5] Chang, W. R., Etsion, I., and Bogy, D. B., 1987, "An Elastic-Plastic Model for the Contact of Rough Surfaces," ASME J. Tribol., **109**, pp. 257–263.
[6] Zhao, Y., Maletta, D. M., and Chang, L., 2000, "An Asperity Microcontact Model Incorporating the Transition From Elastic Deformation to Fully Plastic Flow," ASME J. Tribol., **122**, pp. 86–93.
[7] Jacq, C., Nelias, D., Lormand, G., and Girodin, D., 2003, "Development of a Three-Dimensional Semi-Analytical Elastic-Plastic Contact Code," ASME J. Tribol., **125**, pp. 653–667.
[8] Vu-Quo, L., Zhang, X., and Leesburg, L., 2000, "A Normal Force-Displacement Model for Contacting Spheres Accounting for Plastic Deformation: Force Driven Formulation," ASME J. Appl. Mech., **67**, pp. 363–371.
[9] Abbott, E. J., and Firestone, F. A., 1933, "Specifying Surface Quality-A Method Based on Accurate Measurement and Comparison," Mech. Eng. (Am. Soc. Mech. Eng.), **55**, pp. 569–572.
[10] Greenwood, J. A., and Tripp, J. H., 1971, "The Contact of Two Nominally Flat Rough Surfaces," Proc. Inst. Mech. Eng., **185**, pp. 625–633.
[11] Tabor, D., 1951, *The Hardness of Materials*, Clarendon Press, Oxford.
[12] Davis, J. R., 1999, *Metals Handbook*, 2nd ed., ASM International, Metals Park, OH.
[13] Francis, H. A., 1976, "Phenomenological Analysis of Plastic Spherical Indentation," ASME J. Eng. Mater. Technol., **98**, pp. 272–281.
[14] Oliver, W. C., and Pharr, G. M., 1992, "An improved technique for determining hardness and elastic modulus using load and displacement sensing indentation," J. Mater. Res., **7**(6), pp. 1564–1583.
[15] Mesarovic, S. D., and Fleck, N. A., 2000, "Frictionless Indentation of Dissimi-

lar Elastic-plastic Spheres,'' Int. J. Solids Struct., **37**, pp. 7071–7091.
[16] Kral, E. R., Komvopoulos, K., and Bogy, D. B., 1993, ''Elastic-Plastic Finite Element Analysis of Repeated Indentation of a Half-Space by a Rigid Sphere,'' ASME J. Appl. Mech., **60**, pp. 829–841.
[17] Kral, E. R., Komvopoulos, K., and Bogy, D. B., 1995, ''Finite Element Analysis of Repeated Indentation of an Elastic-Plastic Layered Medium by a Rigid Sphere, Part I: Surface Results,'' ASME J. Appl. Mech., **62**, pp. 20–28.
[18] Kral, E. R., Komvopoulos, K., and Bogy, D. B., 1995, ''Finite Element Analysis of Repeated Indentation of an Elastic-Plastic Layered Medium by a Rigid Sphere, Part II: Subsurface Results,'' ASME J. Appl. Mech., **62**, pp. 29–42.
[19] Streator, J. L., 2003, ''Dynamic Contact of a Rigid Sphere With an Elastic Half-Space: A Numerical Simulation,'' ASME J. Tribol., **125**, pp. 25–32.
[20] Tian, H., and Saka, N., 1991, ''Finite element analysis of an elastic-plastic two-layer half-space: normal contact,'' Wear, **148**, pp. 47–68.
[21] Johnson, K. L., 1985, *Contact Mechanics*, Cambridge University Press, Cambridge.
[22] Giannakopoulos, A. E., Larsson, P. L., and Vestergaard, R., 1994, ''Analysis of Vickers Indentation,'' Int. J. Solids Struct., **31**, pp. 2679–2708.
[23] Barber, J. R., and Ciavarella, M., 2000, ''Contact Mechanics,'' Int. J. Solids Struct., **37**, pp. 29–43.
[24] Liu, G., Wang, G. J., and Lin, C., 1999, ''A Survey of Current Models for Simulating the Contact between Rough Surfaces,'' Tribol. Trans., **42**, pp. 581–591.
[25] Johnson, K. L., 1968, ''An Experimental Determination of the Contact Stresses Between Plastically Deformed Cylinders and Spheres,'' Engineering Plasticity, Cambridge University Press, Cambridge, pp. 341–361.
[26] Reddy, J. N., 1993, *An Introduction to the Finite Element Method*, 2nd ed., McGraw-Hill, New York.
[27] Shigley, J. E., and Mischke, C. R., 1989, *Mechanical Engineering Design*, 5th ed., McGraw-Hill, New York.
[28] Quicksall, J., Jackson, R. L., and Green, I., 2004, ''Elasto-plastic Hemispherical Contact for Varying Mechanical Properties,'' accepted for publication in J. Eng. Tribol.-Part J.
[29] Williams, J. A., 1994, *Engineering Tribology*, Oxford University Press, Oxford.
[30] Goodier, J. N., and Hodge, P. G., 1958, *Elasticity and Plasticity*, Wiley, New York.
[31] Chang, W. R., 1986, ''Contact, Adhesion, and Static Friction of Metallic Rough Surfaces,'' Ph.D. thesis, University of California, Berkeley, pp. 18–23.